Appendix

Description of Research Projects

1) Modeling of Nonlinear Active and Passive Devices in Three-Dimensional TLM Networks

(Lucia Cascio, Giampaolo Tardioli and Wolfgang J.R. Hoefer)

The increase in clock rate and integration density in modern IC technology leads the designer to deal with problems for which traditional lumped circuit design methodology fails to accurately account for the complex interactions among different parts of the circuit. Traditional CAD tools, such as SPICE, provide very accurate models for a large variety of active devices, but their description of the passive part of the circuit is progressively becoming insufficient as the frequencies of the signals increase. Problems such as dispersion, crosstalk and package effects require a full electromagnetic approach in order to predict their impact on the final response of the circuit.

The TLM method is particularly suitable for interfacing lumped circuits to distributed structures: the electromagnetic fields are directly related to the voltages and currents propagating in the TLM transmission lines, and it is straightforward to interpret the connection between the distributed electromagnetic problem and the lumped devices in terms of circuit theory. Moreover, unlike FDTD, the TLM method is very stable at low frequencies, particularly in the presence of one-way absorbing boundary conditions.

We have thus developed a technique for introducing lumped elements in a set of TLM-SC nodes. To incorporate the circuit into the TLM mesh, we consider an equivalent region extending over the device volume, and we assume that the behavior of the device depends on the local field in all the cells in that volume. This is particularly important in the case of nonlinear active elements, such as Tunnel diodes, because the connection of the cells in the direction of the feeding voltage would have the effect of a series of diodes, which is DC-unstable. A second advantage is that when modeling nonlinear devices such as pn-junction diodes or bipolar transistors, we will need to solve only a single nonlinear equation at each iteration.

To connect the device to the TLM mesh we add *n* series-connected capacitive stubs in the direction of the feeding voltage. The inclusion of the circuit into the TLM mesh is performed by expressing the equation relating the voltage across the element, *v*, and the current flowing into it, *i*, as a function of the voltages traveling in the TLM stubs:

$$v = \sum_{m=1}^{n} v_m = \sum_{m=1}^{n} (v^i_m + v^r_m)$$

$$i = i_m = Y_r (v^r_m - v^i_m) \qquad m = 1, \ldots, n$$

Substituting the expressions for the current and for the voltage in the equation describing the lumped

circuit, and applying an appropriate discretization scheme, we obtain a recursive formulation for the new incident voltages traveling in the stubs. For first-order circuits this can be written as:

$${}_kV^i_{s1} = F\left[{}_kV^r_{s1},\ {}_{k-1}V^i_{s1},\ {}_{k-1}V^r_{s1},\ \sum_{m=2}^{n} {}_kV^r_{sm},\ \sum_{m=2}^{n} {}_{k-1}V^r_{sm}\right]$$

$${}_kV^i_{sm} = {}_kV^r_{sm} - {}_kV^r_{s1} + {}_kV^i_{s1} \qquad m = 2, \ldots, n$$

The proposed technique has been specialized for several kinds of circuits, and has proven to be capable of correctly describing the transient response of nonlinear devices, including the DC behavior of active elements..

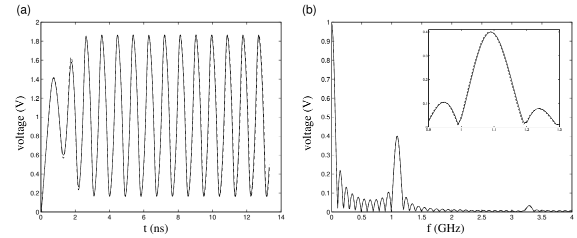

Fig. 1 Time (a) and frequency (b) response for one of the diodes in the stripline oscillator (Solid line: SPICE, dashed line: TLM)

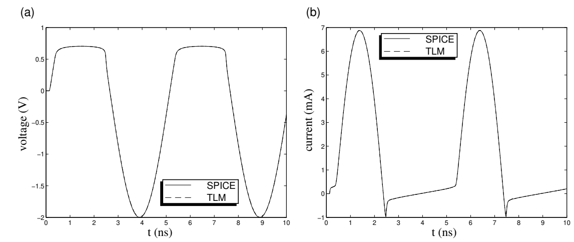

Fig. 2 Voltage (a) and current (b) behavior for the pn-junction diode: comparison between the TLM simulation and SPICE results

We have simulated an air-filled stripline oscillator with its DC biasing circuit. The time and frequency behavior of the oscillator, determined with the TLM analysis, has been compared with a SPICE simulation

(Fig. 1). The difference between the SPICE and the TLM simulations during the transient period is due to the adaptive time-step used by SPICE. The frequency response in Fig. 1 Fig. 1(b) has been evaluated after the steady-state condition has been reached (t > 2.915 ns).

As a second example we have modeled the dynamic behavior of a pn-junction diode placed at one extremity of a stripline. The TLM analysis of the given structure has been compared with the results obtained using SPICE (Fig. 2Fig. 2), showing an excellent agreement both for the voltage and current behavior

Further details can be found in:

L. Cascio, G. Tardioli and W. J. R. Hoefer, “Modeling of Nonlinear Active and Passive Devices in Three-Dimensional TLM Networks”, in IEEE Intl. Microwave Symp. Dig, pp. 383-386, Denver, Colorado, June 8-13, 1997.

2) Special 3D-TLM Corner Nodes for Singular Field Regions

(Giampaolo Tardioli, Lucia Cascio, Mario Righi, and Wolfgang J.R. Hoefer)

Introduction

Space discrete methods such as Finite Difference Frequency Domain (FDFD), Finite Difference Time Domain (FDTD), Transmission Line Matrix (TLM) and Finite Element Methods (FEM), are currently used for solving a wide variety of fields problems. The computational domain is discretized in a finite number of elementary cells where the electromagnetic field is assumed to have a simple behavior, very often linear. This assumption fails to accurately model sharp features, where highly nonuniform fields are present. This is typically the case of corners and edges, where the electromagnetic fields are singular. We refer to the resulting error as “coarseness error”.

In time domain methods, a comparison between the dispersion and the coarseness error reveals that the coarseness error is the dominant source of inaccuracies in most of the practical cases and represents the most severe limitation to the maximum admissible cell size.

A direct solution to reduce the coarseness error is to use an extremely fine mesh, but this quickly leads to unacceptable memory and time requirements. A better approach is to use a variable or multigrid mesh, so that a higher resolution can be obtained in that region. In this case the resources would be still larger than those of a uniform coarser mesh fixed by the dispersion error only.

We present a novel approach to incorporate knowledge of the static field behavior in the vicinity of singularities in a three-dimensional TLM mesh. The procedure is systematic and does not require optimization of the correcting elements. As a result, relatively coarse TLM meshes may be used to obtain highly accurate results, within the dispersion error, across a wide frequency range.

Theoretical Background

Close to edges (Fig. 1) the spatial derivatives of the fields are much larger than the time derivatives, so that the latter may be neglected in Maxwell’s equations. Therefore the propagation effects are negligible and the electromagnetic field is quasi-static. The finite energy condition imposes that the **E** and **H** field

components normal to the corner become singular, while the **E** and **H** tangential components remain finite.

In particular, for a knife wedge (α=0), the y-field components can be expressed as:

$$E_y(r, \phi, t) = \alpha(t)\, r^{1/2} \sin\left(\frac{\phi}{2}\right) + \beta(t) \cdot r \cdot \sin(\phi) + \gamma(t)\, r^{3/2} \sin\left(\frac{3}{2}\phi\right) + \ldots \qquad (1)$$

$$H_y(r, \phi, t) = c_0(t) + c_1(t) \cdot r^{1/2} \cdot \sin\left(\frac{\phi}{2}\right) + c_2(t)\, r \sin(\phi) + \ldots \qquad (2)$$

Considering Maxwell’s equations written in the cylindrical coordinate system *y*-r-ϕ, we obtain:

$$\frac{\partial H_r}{\partial y} - \frac{\partial H_y}{\partial r} = \varepsilon_0 \frac{\partial E_\phi}{\partial t} \qquad \frac{\partial E_r}{\partial y} - \frac{\partial E_y}{\partial r} = -\mu_0 \frac{\partial H_\phi}{\partial t} \qquad (3)$$

where Ey and Hy in the vicinity of the corner are given by (1)(1), and (2)(2).

Edge Singularity, TM-Polarization

Consider the case of the knife edge embedded in a TLM mesh as depicted in Fig. 2.

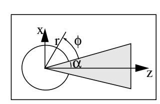

Fig. 1Perfectly conducting wedge

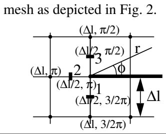

Fig. 2Knife edge in a TLM mesh; the edge is placed on TLM nodes

We want to implement the equations (3) including the edge condition (1) and (2) at the three TLM link lines. In particular for the TMy polarization (Hy=0), we have:

$$\mu_0 \left.\frac{\partial H_\phi\left(\frac{\Delta}{2}, \phi, t\right)}{\partial t}\right|_{\phi = \frac{\pi}{2}, \pi, \frac{3}{2}\pi} = \left.\frac{\partial E_y\left(\frac{\Delta}{2}, \phi, t\right)}{\partial r}\right|_{\phi = \frac{\pi}{2}, \pi, \frac{3}{2}\pi} - \left.\frac{\partial E_r\left(\frac{\Delta}{2}, \phi, t\right)}{\partial y}\right|_{\phi = \frac{\pi}{2}, \pi, \frac{3}{2}\pi} \qquad (4)$$

Replacing the time derivative with the central difference scheme, recalling the mapping between voltages and fields between link lines in the 3D-SCN node, and using the static expansion in (2) we obtain the following modified scattering procedure for higher-order approximation:

$$G(\phi, k) = \frac{1}{2}\alpha(k\Delta t)\left(\frac{\Delta l}{2}\right)^{-\frac{1}{2}} \sin\left(\frac{\phi}{2}\right) + \beta(k\Delta t)\sin(\phi) + \frac{3}{2}\gamma(k\Delta t)\left(\frac{\Delta l}{2}\right)^{\frac{1}{2}} \sin\left(\frac{3}{2}\phi\right)$$
$$V^r_k = V^i_k + V^r_{k-1} - V^i_{k-1} + \frac{\Delta l^2}{2} \cdot \left(G(\phi, k) - \frac{\partial E_r}{\partial y}\right) \qquad (5)$$

where Z0 is link line characteristic impedance, V_k^r are the voltage pulses incident on the points 1,2,3 from *the corner node* and V_k^i are the voltage pulses incident on the points 1,2,3 from *the external nodes* at the *kth* iteration.

The coefficients α(t), β(t), γ(t) are unknown. Their value can be determined by evaluating the electric field *Ey* at the three adjacent nodes at each time step and solving a linear system.

Similar calculations can be carried out for the TE polarization, obtained a modified scattering procedure similar to that depicted in the previous formula.

Results

In order to validate the proposed approach for the two different polarizations, we have implemented the algorithm in the 3D-SCN node, and computed the first resonant frequency of the cavities depicted in Fig. 3 and Fig. 4. The first structure is a rectangular cavity with an asymmetric inductive iris in the center.

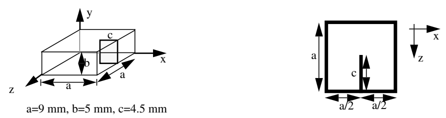

Fig. 3Resonant cavity in rectangular waveguide with inductive coupling

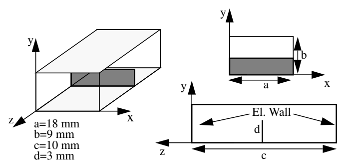

Fig. 4Resonant cavity in parallel plate waveguide with capacitive coupling

The second structure is a parallel plate waveguide resonator with an asymmetric capacitive iris in the middle. In both situations the new method as been compared with results available in the literature and with those obtained with the standard TLM algorithm with increasingly small discretization steps. Even with a very coarse mesh the introduction of the static-field correction yields an improvement in the accuracy with negligible impact on the computational time; the percentage error is reduced from 3.8% to 1% in the case of the TM polarization (Table 1), and from 10% to 0.3% in the case of TE polarization (Table 2). These results are consistent with those obtained with a standard TLM algorithm with cell sizes five to six times smaller with a significant saving in computational effort.

Table 1 Inductive Iris cavity resonant frequencies (GHz)

Δl	1 mm	1/3 mm	1/5 mm
TLM	31.732	31.062	30.922
Marcuvitz	30.560	-	-
Static Correction	30.889	-	-

Table 2 Capacitive Iris Cavity Resonant Frequencies (GHz)

Δl	1 mm	1/3 mm	1/5 mm	1/11 mm
TLM	11.175	11.935	12.105	12.260
Marcuvitz	12.475	-	-	-
Static Correction	12.510		-	-

Conclusion

A novel systematic procedure to incorporate static field configuration into a 3D-TLM mesh has been proposed. The method introduces the correct field singularity by exploiting the previous incident and reflected link-line voltages surrounding the corner node. The procedure requires negligible additional operations and leads to a saving in computational time and memory of two orders of magnitude.

Further details can be found in:

G. Tardioli, L. Cascio, and W. J. R. Hoefer, "Special 3D-TLM Corner Nodes for Singular Field Regions", in 1997 IEEE MTT Symposium Dig., pp. 317-320, Denver, Colorado, June 9-13, 1997.

3) Characterization of Surface Mount Package Effects with the TLM Method

(Giampaolo Tardioli, Mario Righi, Lucia Cascio, and Wolfgang J. R. Hoefer)

Introduction

A typical problem facing designers of integrated circuits is to determine the effect of the package on the performance of a monolythic microwave integrated circuit (MMIC) it contains. The presence of leads, bond wires and grounding pins affects the MMIC behavior. These effects must be included in the early design stages. In order to avoid costly design cycles, an electromagnetic approach becomes attractive to predict accurately the performances of a packaged circuit.

We have performed the full wave time-domain analysis of a surface mount plastic package containing a simplified MMIC (a thru connection and a microstrip spiral inductor). Problems such as poor grounding terminations and crosstalk with neighboring lines are also considered as they can occur at relatively low frequencies.

Finally, we propose an approach to isolate the package effects. The whole structure is segmented and the package is characterized by its scattering parameters. In this way the package needs only to be modeled once for a given configuration. The package effects are extracted and combined with the MMIC parameters to predict the performance of the packaged circuit at a fraction of the computational costs. In addition, the MMIC circuit can be optimized by including the package effects from the design stages, thus signifi-

cantly reducing costly cut-and-try cycles.

TLM Analysis of the SOIC-8 Package

The described critical issues appear in the analysis of the SOIC-8 surface mount package. The structure comprises 8 leads which allow the IC to be soldered onto the mother-board. Some of the leads are extended to the paddle to provide grounding to the MMIC, while other leads are connected by bond wires to the MMIC providing input and output to the circuit. The geometry of the structure is shown in Fig. 5.

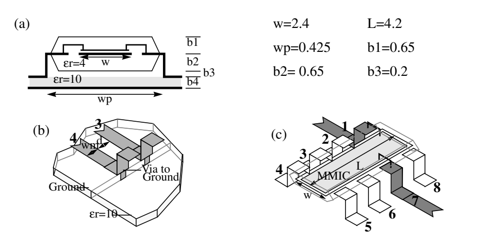

Fig. 5 Plastic Package dimensions and geometrical details. All dimensions are in mm. (a) Package section (b) Detail of the grounding to the mother-board (c) MMIC mounted on the plastic package

Poor Grounding

In order to highlight the effects of the grounding leads, a microstrip spiral inductor has been analyzed under poor grounding characteristics (Fig. 6a). In this case the configuration was: leads 1 and 5 provide input and output to the spiral; all other leads are grounded on the mother-board by means of vias, but only leads 4 and 8 are extended to provide ground on the package. Poor ground was simulated by assuming a faulty solder connection on one of the vias so that either via no. 4 or via no. 8 is ineffective.

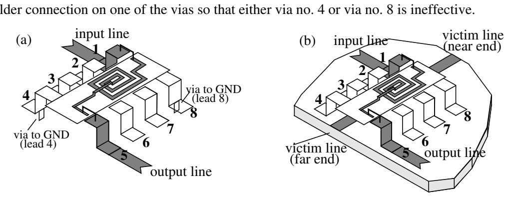

Fig. 6 (a) Geometry of the microstrip spiral inductor under poor grounding conditions (either via on lead 4 or 8 are made ineffective. (b) Geometry of the package with a microstrip line beneath it to evaluate crosstalk.

Results are shown in Fig. 7. The results for the two cases of ineffective vias are overlapping and only one of the two is shown. This similarity can be explained considering the high degree of symmetry of the

structure. Note that a poor ground reduces the bandwidth of operation of the inductor by 500 MHz because of the additional inductance provided by the longer path of the return currents.

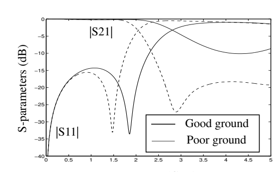

Fig. 7 Scattering parameters for the microstrip spiral inductor on the MMIC under good and poor grounding conditions

Crosstalk

The same microstrip inductor has been used to evaluate the presence of crosstalk between the input line and a crossing microstrip on the mother-board (Fig. 6b). A transient analysis of the problem has been performed and the time domain waveforms coupled to the victim crossing line have been extracted. The The voltage transmission coefficients to the victim line are shown in Fig. 8. Note that an unexpected amount of power is coupled on the near end. In the frequency range from 7 to 9 GHz as much as 13% of the voltage is transferred to the victim line.

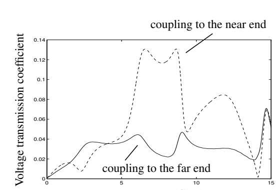

Fig. 8 Voltage transmission coefficient from the input line to the victim line for the configuration in Fig. 6b.

Segmentation

In order to isolate the package effect, we have segmented the structure into 3 sections. A first section consisting of the microstrip on the mother-board, the transition to the package, the bonding wire and the initial section of the MMIC. A second section composed of the MMIC itself; in this case a thru connection and a microstrip spiral inductor. A third section, similar to the first, to provide transition to the output line on the mother-board. The process is illustrated in Fig. 9, where the dashed lines represent the reference planes at which the segmentation was operated.

The scattering parameters of the segmented structure and of the full structure for the two cases are shown in Fig. 10. From these results it appears that the proposed approach is reliable in the frequency range dc to ~4 GHz. Above this frequency, the assumption of single mode interaction between the different sections fails to accurately describe the overall behavior of the circuit thus requiring a more sophisticated multi-port approach.

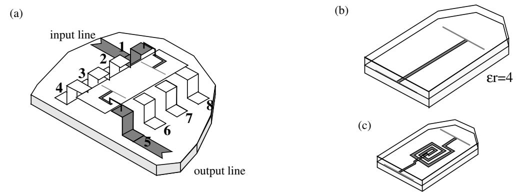

Fig. 9 Segmented structure: (a) input and output sections, (b) embedded thru connection, (c) embedded spiral inductor. The dashed lines represent the reference planes.

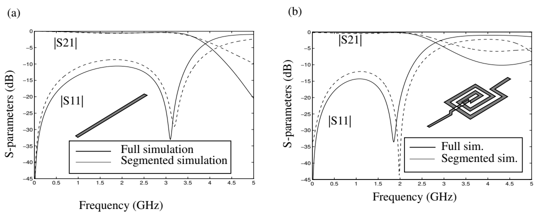

Fig. 10 Scattering parameters of the segmented structure compared with those of a full simulation; (a) thru connection, (b) spiral inductor.

Conclusion

The full wave analysis of a surface mount plastic package containing a test MMIC has been presented. The need for a full wave tool to characterize the package effect is highlighted, and valuable insight into the behavior of the packaged MMIC is gained. Poor grounding conditions have shown to change significantly the performance of the circuit, and crosstalk with crossing lines cannot be neglected.

A segmentation approach has also been proposed. The package effects have been extracted and combined with MMIC parameters to predict the performance of the packaged circuit at a fraction of the computational costs. In addition, the MMIC circuit can be optimized by including the package effects from the design stages.

Further details can be found in:

M. Righi, G. Tardioli, L. Cascio, W. J. R. Hoefer, "Time Domain Characterization of Packaging Effects via Segmentation Technique" to be published on the Special Issue on Packaging Effects and Interconnects of the MTT-S IEEE Transactions, September 1997.

4) Modal Boundary Conditions for Waveguides of Arbitrary Cross-section with SCN TLM

(Jonathan Herring, Mario Righi, Wolfgang J. R. Hoefer)

Modal absorbing boundary conditions have been applied to a graded mesh using the hybrid node, and to homogeneous waveguides of arbitrary cross-section. The best performance is obtained with rectangular waveguides but examples show that the method can also be used for other geometries. A T-junction circular-to-sidecoupled rectangular waveguide example is given.

For rectangular waveguides, the modal field distribution is well known. In the application of modal boundary conditions to TLM, it is convenient to work directly with the voltage pulses, rather than with the total tangential field components. This is possible because the link-line voltages are a linear combination of the electric and magnetic fields. For a graded mesh using the hybrid node, three different impedances are assigned to the three sets of link-lines contributing to each component of the magnetic field. The modal Green's function is determined by the timestep and the node dimension perpendicular to the boundary; it is independent of the mesh grading in the cross-section.

Typical Green's functions for the dominant mode in a WR28 waveguide are shown in the frequency domain in fig. 1, for the cases of (*i*) cubic nodes with the maximum timestep, (*ii*) cubic nodes with half the maximum timestep, and (*iii*) cuboid nodes of twice the length in the perpendicular direction and with the maximum timestep.

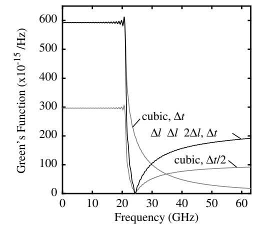

Fig. 1 – Modal Green's functions for hybrid node

As the frequency increases, the curves tend towards the link-line reflection coefficient needed to match the TLM mesh to free-space:

$$\rho_l = \frac{\Delta l_{min} - \Delta l}{\Delta l_{min} + \Delta l} \qquad \text{where} \qquad \frac{l_{imn}}{t} = 2c\ \Delta t$$

Δl is the perpendicular node spacing, Δt is the timestep and c is the speed of light.

For homogeneous waveguides of arbitrary cross-section, the mode configuration can be obtained from two previous two-dimensional simulations. It is convenient to use a slice of three-dimensional nodes for this purpose. The cutoff frequencies are obtained from the first simulation and then, in the second, the Fourier transform of the appropriate voltage pulses is computed at these frequencies over the whole plane.

To form the modal coupling matrix, the complex output from the Fourier transform must be converted to real numbers. The magnitude can be taken if the field is orientated in a single direction. The resulting matrix can be used directly to convert from mode amplitudes to TLM voltage pulses. To convert back to mode amplitudes, a new matrix is formed in which each element is multiplied by the area of the corresponding node, and then a scaling factor is applied so that the conversions *to modes* and *from modes* are consistent. The voltage pulses incident on the boundary are then multiplied by the elements of this matrix.

The reflection coefficient of practical ABC's can be calculated as an S-parameter, from a knowledge of the total voltage and the incident voltage at the input port. The reference structure is used to obtain the incident voltage, and the length is chosen so that voltage pulses reflected from the ends of the waveguide are not visible at the output point, within the duration of the simulation.

Typical results are shown in fig. 2 for a ridged waveguide modelled at two different resolutions (32 by 16 nodes and 64 by 32 nodes) and for a circular waveguide.

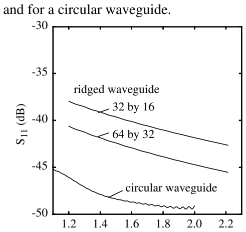

Fig 2 – Spurious reflection coefficient for ridged and circular waveguides terminated with modal ABC's

For rectangular waveguides, the performance of modal ABC's approaches the limit of numerical precision. Spurious reflections as low as -120dB are obtained with single precision arithmetic and -300dB with double precision.

The ABC's for uniform waveguides of arbitrary shape have been applied to the circular ports of the circular-to-rectangular T-junction shown in fig. 3a. A standard modal ABC for rectangular waveguides was used on port 3. Only the dominant modes were considered. The ABC's were therefore placed away from the junction, to ensure that all higher order modes would be sufficiently decayed. The entire

structure was discretized on a cubic mesh with 28 cells in the diameter of the circular waveguide. The S-parameters are shown in fig. 3b, along with results obtained with a mode matching approach. Similar TLM results can be obtained with one-way equation ABC's, although there is always the potential for instabilities with this type of boundary.

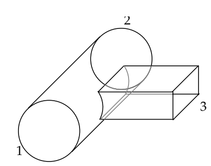

Fig.3a – Geometry of the circular to sidecoupled rectangular waveguide T-junction. Radius: 7.0 mm, rectangular waveguide: WR-62 (16.0 mm by 8.0 mm)

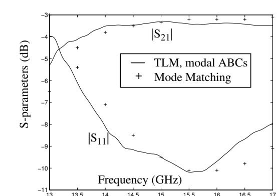

Fig.3b – Magnitude of the S-parameters of the circular to sidecoupled rectangular waveguide T-junction.

Further details can be found in:

J. L. Herring, M. Righi, W.J.R. Hoefer, "Modal Boundary Conditions For Waveguides of Arbitrary Cross-section With SCN TLM" in 1997 Intl. Microwave Symposium Dig., pp. 325-328, Denver, Colorado, June 9-13, 1997.

5) RF drying of softwood lumber in collaboration with the Faculty of Wood Science in UBC

(Mario Righi, Jonathan Herring, Wolfgang J. R. Hoefer and UBC team)

In the course of this research project a time domain model for the RF drying of wood in a vacuum kiln has been developed. The model includes the following physical phenomena involved in the drying of wood:

- Electromagnetic field distribution in the wood and the surrounding kiln,
- Energy deposition which increases the mobility of moisture in the lumber,
- Heat transfer and
- Mass transfer which, in turn, changes the dielectric properties of the wood.

The project aims at coupling all these phenomena in a self-consistent numerical model in space and time. Validation of the simulated results will be performed using the experimental RF/Vacuum Kiln available at UBC.

In order to cast the numerical models into a form directly amenable to experimental verification, the algorithms were implemented for a geometry resembling that of the UBC experimental kiln which is shown in Fig. 1. For modeling convenience, the parallel plates containing the wood sample were placed in a rectangular rather than circular cavity.

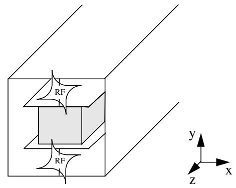

Figure 1. UBC RF kiln

The size of the wood sample is about 1 by 1 by 8 feet. Symmetry along the three axes has been exploited: only one-eighth of the structure needs to be considered, which leads to considerable savings. The electromagnetic as well as the thermal and mass transfer models are stand-alone FORTRAN programs which can exploit public domain plotting routines for interactive visualization (e.g. PLPLOT).

The algorithm modeling the interaction between the electromagnetic solver and the heat/moisture diffusion solver is shown in Fig. 2.

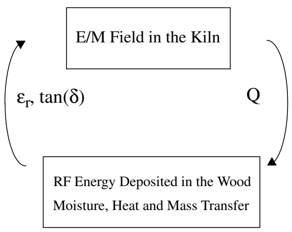

$$\nabla \times \boldsymbol{E} = -\frac{\partial}{\partial t}(\mu_r \boldsymbol{H})$$

$$\nabla \times \boldsymbol{H} = \boldsymbol{j} + \frac{\partial}{\partial t}(\varepsilon_r \boldsymbol{E})$$

$$\frac{\partial M}{\partial t} = \nabla (D_M \nabla M) + \nabla (D_T \nabla T)$$

$$\rho c \frac{\partial T}{\partial t} = \nabla (\lambda_T \nabla T) + \nabla (\lambda_M \nabla M) + Q$$

Figure 2 Modeling algorithm for the coupled electromagnetic/heat diffusion/moisture diffusion phenomena, and the differential equations governing them.

The algorithm can be summarized as follows:

a) The thermal mesh and the EM mesh are arranged so that they overlap each other;

b) The electromagnetic field, temperature and moisture are available in each cuboid mesh cell, at each time step;

c) The electromagnetic field in every point in the kiln is computed with TLM;

d) The RF power dissipated in each cuboid is fed as source into the thermal code;

e) One time step at a time in the thermal code is performed (diffusion of heat and moisture) in the wood until a change in material parameters (ε' and tan(δ) is detected;

f) The new parameters are returned to the electro-magnetic TLM code to generate the new field configuration.

These cycle is repeated until the wood is dry.

Characteristics of the Electromagnetic Code

The electromagnetic code is based on the TLM method in the cuboid formulation. Stubs are added to the elementary node in order to model the anisotropic properties of the wood. Because the placement of the wood in the kiln usually aligns the wood fibers with the kiln axis, only diagonal tensors for the permittivity and permeability are necessary. Time varying ε' and tan(δ) are con-sidered and can be specified through interpolated functions (related to the temperature and moisture content in that region of wood) or by look-up tables. In this way different wood species and other biopolymers can be modeled. Boundary conditions are given by the kiln and electrode geometry.

Characteristics of the Thermal Code

The thermal code model is a discrete formulation of the heat and moisture diffusion processes. The equations governing these processes are given in the lower right quadrant of Figure 2. In these equa-tions ρ is the wood density, c is the wood specific heat, T is the temperature in the wood, M is the moisture content and Q is the heat deposited by the radio frequency electromagnetic fields. The coefficients D_M, D_T, λ_M, λ_T are the diffusivity coefficients for the moisture content and the heat.

The presence of these coefficients means that the heat and moisture diffusion can occur because of the gradients of both heat and moisture. Based on the input received by Dr. Avramidis and his group at UBC the equations can be simplified as:

$$\frac{\partial M}{\partial t} = \nabla (D_M \nabla M)$$

$$\rho c \frac{\partial T}{\partial t} = \nabla (\lambda_T \nabla T) + Q$$

The above differential equations have been discretized using Finite Differences in the Time Domain (FDTD) based on the FTCS (Forward Time Central Space) scheme. Cuboid nodes and anisotropic properties (diagonal tensor) have been implemented. Inhomogenous regions are also considered. All above parameters can be time varying, and can be specified as functions of moisture, temperature, fiber saturation point, etc. either as look-up tables or as specified functions.

As the diffusion evolves, the dielectric properties of the material change, and the new properties are fed back to the electromagnetic solver to compute the new field distribution. In order to ensure an accurate tracking of the field as it evolves in the wood, only small changes in moisture and temperature distribution are allowed. This is accomplished by using an adaptive time step for the diffusion phenomena. The time step at each iteration of the thermal code is computed so that the change in properties is smaller than 1%.

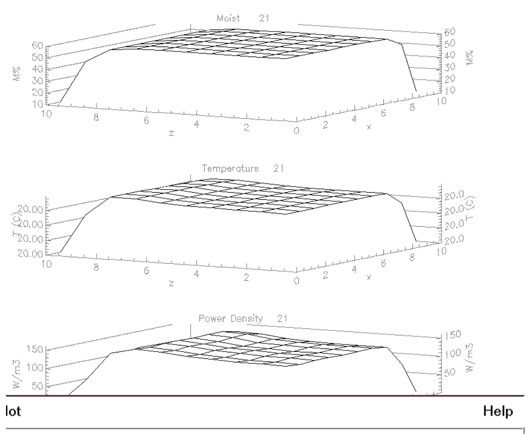

Figure 3. Moisture, temperature and power density in 1/8 of the wood sample at time step 21.

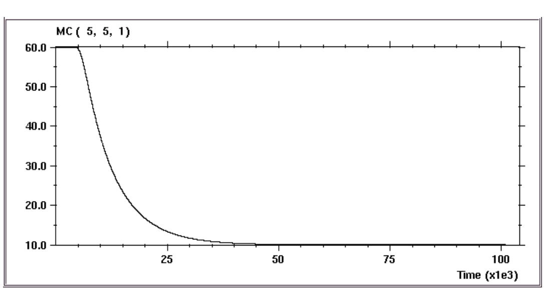

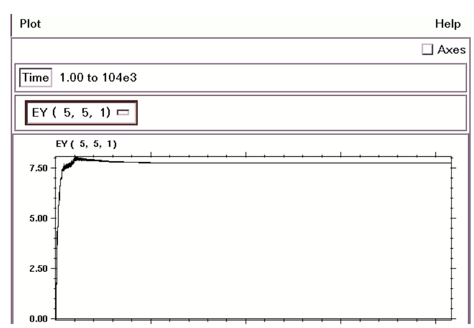

Figure 4. Results obtained during step 1. Constant parameters. Moisture content in % (previous page) and electric field strength at a point in the wood sample.

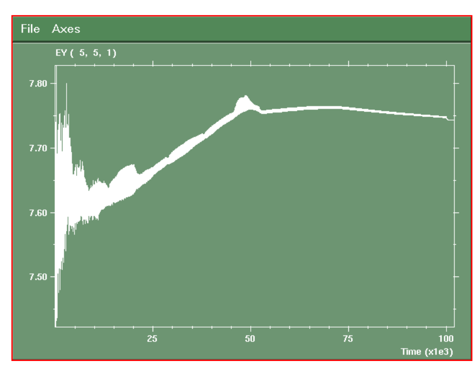

Figure 5. Results obtained during step 2. Variable parameters. Electric field strength at a point inside the wood sample.

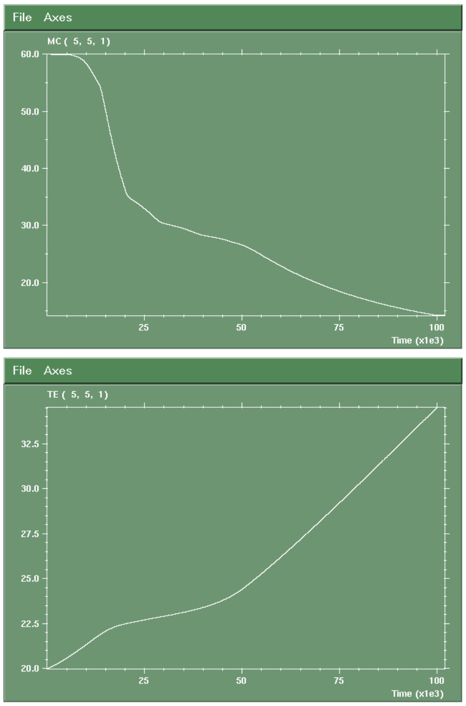

Figure 6. Results obtained during step 2. Variable parameters. Moisture content in % and temperature at a point in the wood sample.

In this way fast and slow diffusion can be always tracked with a suitable time step. The time step can therefore change during the duration of the simulation, while always remaining below the stability limit for the difference scheme given by:

$$\Delta t_{max} \leq \frac{1}{2\left(\frac{D_x}{\Delta x^2} + \frac{D_y}{\Delta y^2} + \frac{D_z}{\Delta z^2}\right)} \qquad \text{Moisture diffusion}$$

$$\Delta t_{max} \leq \frac{1}{2\left(\frac{\lambda_x}{\Delta x^2} + \frac{\lambda_y}{\Delta y^2} + \frac{\lambda_z}{\Delta z^2}\right)} \qquad \text{Heat diffusion}$$

The boundary conditions are imposed according to the initial temperature and moisture in the wood.

Results can be shown interactively, or at the end of the simulation. Figure 3 shows a typical interactive plot showing the moisture, temperature and power density in 1/8 of the wood sample. The initial phases of the diffusion can clearly be identified.

The development of the linkage between the thermal and electromagnetic codes was pursued in two steps. In step one, the thermal and electromagnetic codes were connected while maintaining all parameters in the diffusion equations constant. Results obtained under this simplified condition are shown in Figure 4.

In step two, time-varying, non-constant parameters were used in the diffusion equations to represent the actual process. Results for this conditions are shown in Figures 5 and 6. While these results show a physically consistent behavior, their accuracy depends critically upon the accuracy with which the diffusion parameters can be determined. Research and experimental investigations are in progress at UBC in order to gain more confidence in the accuracy of these results. The plan is to run careful measurements in UBC's experimental RF/Vacuum Kiln. This kiln is presently being fitted with a new power amplifier as energy source, and with new matching networks to maximize power transfer to the sample. During experiments, incident RF power will be kept constant, pressure and temperature are monitored locally, and moisture content will be measured globally in the sample.